Journal of Engineering Mathematics **35:** 339–357, 1999.

Unsteady viscous flow past an impulsively started oscillating and translating elliptic cylinder

S. J. D. D'ALESSIO[1], S. C. R. DENNIS[2] and P. NGUYEN[2]
[1]*Department of Applied Mathematics, University of Waterloo, Waterloo, Ontario, Canada N2L 3G1*
[2]*Department of Applied Mathematics, University of Western Ontario, London, Ontario, Canada N6A 5B7*

Received 26 May 1998; accepted in revised form 3 November 1998

Abstract. The unsteady two-dimensional flow of a viscous incompressible fluid past an impulsively started oscillating and translating elliptic cylinder has been investigated. The governing Navier-Stokes equations expressed in terms of a stream-function/vorticity formulation are solved numerically for the early stages of the flow for moderate to high Reynolds numbers. A boundary-layer type transformation was adopted to scale out the singular nature in the vorticity at the start of the motion. Some comparisons of the flow patterns with the impulsively started translating case have been included to illustrate the effect of oscillation. Wherever possible, comparisons with existing numerical results have been made and the agreement was found to be good.

Key words: viscous, incompressible, two-dimensional, unsteady, elliptic, cylinder.

1. Introduction

The unsteady flow of a viscous incompressible fluid has long been of interest and has been reported in numerous studies. For the case of unsteady two-dimensional flow past a body of cylindrical cross section previous investigations may be divided into the following three categories: theoretical, numerical and experimental. Theoretical work has been conducted for a cylinder started impulsively from rest and subsequently moving with constant velocity in a viscous fluid. For small times after the start the flow can be determined using boundary-layer theory. Blasius [1], Goldstein and Rosenhead [2], Schuh [3], Wundt [4] and Watson [5] have all adopted this approach in the limiting case of infinite Reynolds number, Re, for a circular cylinder. The extension to include finite, but high values of the Reynolds number (based on the diameter of the cylinder) was addressed by Wang [6] and Collins and Dennis [7]. In these investigations the flow variables are expanded in powers of the time from the start of the motion and are consequently restricted to small times after the impulsive start. The underlying basic structure of the initial motion for the case of an elliptic cylinder has been worked out by Staniforth [8].

To advance the solution to larger times the governing unsteady Navier–Stokes equations must be handled numerically. The first numerical solutions, again for the case of the circular cylinder, were performed by Payne [9] for $\mathrm{Re} = 40$, 100 and were integrated to moderate values of the time. This problem was further investigated by Kawaguti and Jain [10], Son and Hanratty [11], Jain and Rao [12], Thoman and Szwezuk [13], Dennis and Staniforth [14] and Collins and Dennis [15]. The more difficult problem involving asymmetric flow has been considered by Patel [16] for the case of the elliptic cylinder while Badr and Dennis [17] have solved the problem of an impulsively started rotating and translating circular cylinder. Lugt and Ohring [18] have solved the pure rotational case of an elliptic cylinder in a viscous fluid

at rest and in a parallel stream. In all of these listed references very small time steps were taken in the integration procedure at the start of the motion due to the singular nature of the impulsive start which we will later expound upon.

The third category is that of unsteady experimental work. Coutanceau and Bouard [19] and Bouard and Coutanceau [20] conducted experiments for the symmetrical case of flow past a circular cylinder while the asymmetrical analog was dealt with by Coutanceau and Menard [21]. The numerical work of Badr and Dennis for Re $= 200$ agrees extremely well with the measurements reported by Coutanceau and Menard. For the flow generated by an impulsively started elliptic cylinder, comparisons between numerical simulation and experimental visualization can be found in Loc *et al.* [22] and Daube *et al.* [23]. Recently, Ohmi *et al.* [24–25] carried out experiments on vortex formation around an oscillating and translating airfoil for Reynolds numbers (based on the chord length) between 1,500 and 10,000.

In the present paper we consider the two-dimensional flow caused by an infinitely long elliptic cylinder set in motion impulsively which translates with uniform velocity U and also undergoes a harmonic oscillation in pitch having a frequency f. The results of this research are of both theoretical and practical importance since it adds to the knowledge of vortex formation and because this problem can be related to several engineering applications. For example, the oscillation in pitch can either be produced by a periodic fluctuation in the external flow or can represent a forced oscillation of the body itself. Some applications corresponding to these possibilities include an airfoil passing through turbulence or the pitching oscillation of a helicopter's rotor. A frame of reference which translates and rotates with the cylinder is employed where the flow variables chosen to describe the motion of the viscous incompressible fluid are taken to be the stream function and the vorticity. The main object of the present study is to obtain numerical solutions of the Navier-Stokes equations for early times which further elaborate the vortex shedding process and how it evolves in time. A numerical technique based on that of Staniforth [8] is utilized and is successful in computing the early development of the flow for moderate to high Reynolds numbers.

The paper is organized as follows. In Section 2 the equations and boundary conditions dictating the flow are presented and a coordinate system which is more appropriate for the geometry considered is introduced. Following this, in Section 3, a boundary-layer type transformation is applied to the equations to better deal with the early structure of the flow. Section 4 outlines a numerical method to solve the transformed set of equations. The results obtained, with emphasis placed on the computed instantaneous flow patterns, are discussed in Section 5 along with a demonstration of convergence of the numerical scheme proposed. Lastly, a brief summary is given in Section 6.

2. Governing equations and boundary conditions

The elliptic cylinder having an axis coinciding with the z-axis is impulsively set into motion at $t = 0$ and is simultaneously subjected to a steady translational motion with speed U in the positive x direction as well as a harmonic oscillation in pitch about the z-axis. The angle of attack, $\alpha(t)$, defined as the angle that the major axis makes with the positive x-axis is chosen to vary according to

$$\alpha(t) = \alpha_0 - \delta \cos(2\pi f t), \tag{1}$$

where δ and f denote the dimensionless amplitude and frequency of oscillation respectively and α_0 refers to the average inclination of the ellipse over one period $T (T = 1/f)$.

In a reference frame that translates and oscillates with the cylinder the elliptic airfoil would be observed to be stationary; however, the flow at large distances would appear to translate and oscillate in an opposite direction to that of the cylinder. In this frame the unsteady dimensionless equations for a viscous incompressible fluid expressed in primitive variables can be written in vector form as

$$\frac{\partial \mathbf{v}}{\partial t} + (\mathbf{v}\cdot\nabla)\mathbf{v} + 2\dot{\mathbf{\Omega}}\times\mathbf{v} + \ddot{\mathbf{\Omega}}\times\mathbf{r} + \dot{\mathbf{\Omega}}\times(\dot{\mathbf{\Omega}}\times\mathbf{r}) = -\nabla P - \frac{2}{\mathrm{Re}}\nabla\times\mathbf{w}, \tag{2}$$

$$\nabla\cdot\mathbf{w} = 0. \tag{3}$$

For two-dimensional flow taking place in the $x-y$-plane we define the velocity $\mathbf{v} = (u, v, 0)$ and the vorticity $\mathbf{w} = \nabla\times\mathbf{v} = (0, 0, \zeta)$. The angular velocity $\dot{\mathbf{\Omega}}$ and angular acceleration $\ddot{\mathbf{\Omega}}$ are given by

$$\dot{\mathbf{\Omega}} = (0, 0, \dot{\alpha}(t)), \qquad \ddot{\mathbf{\Omega}} = (0, 0, \ddot{\alpha}(t)), \tag{4}$$

since the oscillation is about the z-axis. Here, the dot denotes differentiation with respect to time. In Equation (2) $\mathbf{r}$ is the position vector, P is the pressure and Re is the Reynolds number defined as $\mathrm{Re} = 2Uc/\nu$ where ν is the kinematic viscosity and $2c$ is the focal distance. The terms $2\dot{\mathbf{\Omega}}\times\dot{\mathbf{v}}$, $\ddot{\mathbf{\Omega}}\times\mathbf{r}$ and $\dot{\mathbf{\Omega}}\times(\dot{\mathbf{\Omega}}\times\mathbf{r})$ represent noninertial accelerations that must be incorporated into the equations due to the choice of the reference frame; they are known as the Coriolis, transverse and centripetal accelerations, respectively.

Since the flow is two-dimensional it is beneficial to express the governing Navier-Stokes equations in terms of a stream function ψ and scalar vorticity ζ. The dimensionless functions ψ and ζ are related to their dimensional counterparts ψ^* and ζ^* through

$$\psi^* = cU\psi, \qquad \zeta^* = U\zeta/c. \tag{5}$$

In terms of the dimensionless velocity components u, v obtained by dividing the corresponding dimensional components by U we have that

$$u = -\frac{\partial\psi}{\partial y}, \qquad v = \frac{\partial\psi}{\partial x}, \qquad \zeta = -\frac{\partial u}{\partial y} + \frac{\partial v}{\partial x}. \tag{6}$$

In Cartesian coordinates the resulting equations for ψ and ζ assume the following form

$$\frac{\partial^2\psi}{\partial x^2} + \frac{\partial^2\psi}{\partial y^2} = \zeta, \tag{7}$$

$$\frac{\partial\zeta}{\partial t} + 2\ddot{\alpha} = -\frac{\partial\psi}{\partial x}\frac{\partial\zeta}{\partial y} + \frac{\partial\psi}{\partial y}\frac{\partial\zeta}{\partial x} + \frac{2}{\mathrm{Re}}\left(\frac{\partial^2\zeta}{\partial x^2} + \frac{\partial^2\zeta}{\partial y^2}\right), \tag{8}$$

where the dimensionless time t is related to the dimensional time τ through $t = U\tau/c$. The dimensional frequency F is made dimensionless through $F = fU/c$ and is an important parameter in this investigation since it prescribes the relative rotational speed of the tips of the ellipse compared with the translational speed of the flow. Of the three noninertial accelerations previously mentioned, only the transverse acceleration appears in Equation (8).

Because the Cartesian coordinate system is not well suited for numerical work, we introduce the conformal transformation

$$x + iy = \cosh[(\xi + \xi_0) + i\theta], \tag{9}$$

which transforms the contour of the cylinder to $\xi = 0$ and the infinite region exterior to the cylinder to the semi-infinite rectangular strip $\xi \geqslant 0$, $0 \leqslant \theta \leqslant 2\pi$. The constant ξ_0 appearing in Equation (9) is defined by

$$\tanh \xi_0 = \hat{r}, \tag{10}$$

where $\hat{r}$ is the aspect ratio of the elliptic and is equal to the ratio of the minor to major axis. In the transformed coordinates (ξ, θ) Equations (7), (8) become

$$\frac{\partial^2 \psi}{\partial \xi^2} + \frac{\partial^2 \psi}{\partial \theta^2} = H^2 \zeta, \tag{11}$$

$$\frac{\partial \zeta}{\partial t} + 2\ddot{\alpha} = \frac{1}{H^2}\left[-\frac{\partial \psi}{\partial \xi}\frac{\partial \zeta}{\partial \theta} + \frac{\partial \psi}{\partial \theta}\frac{\partial \zeta}{\partial \xi} + \frac{2}{\mathrm{Re}}\left(\frac{\partial^2 \zeta}{\partial \xi^2} + \frac{\partial^2 \zeta}{\partial \theta^2}\right)\right], \tag{12}$$

where H refers to the metric of the transformation given by

$$H^2 = \tfrac{1}{2}[\cosh\, 2(\xi + \xi_0) - \cos\, 2\theta]. \tag{13}$$

The velocity components (v_ξ, v_θ) in the directions of increase of (ξ, θ) now become

$$v_\xi = -\frac{1}{H}\frac{\partial \psi}{\partial \theta}, \qquad v_\theta = \frac{1}{H}\frac{\partial \psi}{\partial \xi} \tag{14}$$

and the vorticity is found through

$$\zeta = \frac{1}{H^2}\left(-\frac{\partial}{\partial \theta}(H v_\xi) + \frac{\partial}{\partial \xi}(H v_\theta)\right). \tag{15}$$

Boundary conditions for ψ and ζ include the no-slip condition

$$\psi = 0, \qquad \frac{\partial \psi}{\partial \xi} = 0 \quad \text{on } \xi = 0 \tag{16}$$

and that of periodicity

$$\psi(\xi, \theta, t) = \psi(\xi, \theta + 2\pi, t), \qquad \zeta(\xi, \theta, t) = \zeta(\xi, \theta + 2\pi, t). \tag{17}$$

At large distances we demand that

$$\exp(-\xi)\frac{\partial \psi}{\partial \xi} \to -\frac{\dot{\alpha}(t)}{4}\, \exp(\xi + 2\xi_0) + \tfrac{1}{2}\, \exp(\xi_0) \sin(\theta + \alpha(t)),$$

$$\exp(-\xi)\frac{\partial \psi}{\partial \theta} \to \tfrac{1}{2} \exp(\xi_0)\, \cos(\theta + \alpha(t)), \qquad \zeta \to -2\dot{\alpha}(t) \quad \text{as } \xi \to \infty. \tag{18}$$

Condition (18) is referred to as the free stream or far-field condition. Because of the reference frame employed these conditions take on a more complicated form which are time dependent. By inspecting the boundary conditions we see that there are two conditions for the stream function on the cylinder surface while none for the vorticity. Later we will discuss a method of handling this situation.

3. Formulation in boundary-layer coordinates

Due to the impulsive start, a singularity in the vorticity at $t = 0$ arises. This can be seen by examining the initial solution of the vorticity transport equation. Immediately after the start the dominant terms in Equation (12) will be given by the balance of

$$\frac{\partial \zeta}{\partial t} = \frac{2}{\mathrm{Re}\, H_0^2} \frac{\partial^2 \zeta}{\partial \xi^2} - 2\ddot{\alpha}(t), \tag{19}$$

where H_0 is the metric evaluated on the cylinder surface $\xi = 0$. The general solution to the above is

$$\zeta(\xi, \theta, t) = \sqrt{\frac{\mathrm{Re}\, H_0^2}{t}}\, \exp\left(-\frac{\mathrm{Re}\, H_0^2 \xi^2}{8t}\right) G(\theta) - 2\dot{\alpha}(t), \tag{20}$$

where $G(\theta)$ denotes an arbitrary function of θ. By examining this solution we see that at $t = 0$ the surface vorticity is infinite where elsewhere the vorticity is zero. This corresponds to an infinitesimally thin ring of vorticity of infinite magnitude generated on the cylinder surface.

Since it is impossible to represent the solution given by (20) numerically at $t = 0$ as required by a numerical scheme, this solution cannot be accurately represented by any finite difference scheme. To overcome this difficulty we make the following boundary-layer type transformation

$$\xi = \lambda z, \qquad \psi = \lambda \Psi, \qquad \zeta = \omega/\lambda, \qquad \lambda = \sqrt{\frac{8t}{\mathrm{Re}}}, \tag{21}$$

which removes the inherent singularity. In this transformation λ denotes the growth of the boundary-layer structure of the initial solution. This change of variables stretches the thin boundary-layer and rescales the stream function and vorticity so that they are of order unity. This transformation has been used by several authors, some of which include Collins and Dennis [15], Staniforth [8], Dennis and Staniforth [14] and Badr and Dennis [17]. In terms of these so-called boundary-layer coordinates Equations (11), (12) now become

$$\frac{\partial^2 \Psi}{\partial z^2} + \lambda^2 \frac{\partial^2 \Psi}{\partial \theta^2} = H^2 \omega, \tag{22}$$

$$\begin{aligned} \frac{1}{H^2}\frac{\partial^2 \omega}{\partial z^2} + 2z\frac{\partial \omega}{\partial z} + 2\omega \;=\; & 4t\frac{\partial \omega}{\partial t} - \frac{\lambda^2}{H^2}\frac{\partial^2 \omega}{\partial \theta^2} \\ & - \frac{4t}{H^2}\left(\frac{\partial \Psi}{\partial \theta}\frac{\partial \omega}{\partial z} - \frac{\partial \Psi}{\partial z}\frac{\partial \omega}{\partial \theta}\right) + 8\lambda t \ddot{\alpha}. \end{aligned} \tag{23}$$

Thus, the early stages of the flow are best described by Equations (22), (23). For later times it may be worthwhile to switch back to the physical coordinates (ξ, θ) once the boundary-layer thickens appreciably. We emphasize that although boundary-layer coordinates are utilized, the full Navier-Stokes equations are to be solved and not the simplified boundary-layer equations.

4. Numerical solution technique

The numerical method implemented to solve Equations (22), (23) is similar to that outlined in Staniforth [8] and will be briefly described below. We begin by discretizing the computational domain bounded by $0 \leqslant z \leqslant z_\infty$ and $0 \leqslant \theta \leqslant 2\pi$ into a network of $N \times M$ grid points located at

$$z_i = ih, \quad i = 0, 1, \ldots, N, \tag{24}$$

$$\theta_j = jk, \quad j = 0, 1, \ldots, M \tag{25}$$

with

$$h = \frac{z_\infty}{N}, \tag{26}$$

$$k = \frac{2\pi}{M}. \tag{27}$$

Here, z_∞ refers to the outer boundary approximating infinity. By placing z_∞ well outside the growing boundary-layer this enables us to enforce the free stream condition (18) along the line $z = z_\infty$. Expressed in terms of the boundary-layer coordinates (z, θ) this condition becomes

$$\exp(-\lambda z)\frac{\partial \Psi}{\partial z} \to -\frac{\dot{\alpha}(t)}{4} \exp(\lambda z + 2\xi_0) + \tfrac{1}{2} \exp(\xi_0) \sin(\theta + \alpha(t)),$$

$$\exp(-\lambda z)\frac{\partial \Psi}{\partial \theta} \to \frac{1}{2\lambda} \exp(\xi_0) \cos(\theta + \alpha(t)), \quad \omega \to -2\lambda\dot{\alpha} \quad \text{as } z \to \infty. \tag{28}$$

We point out that the physical coordinate $\xi = \lambda z$ is a moving coordinate and hence the outer boundary $\xi_\infty = \lambda z_\infty$ is constantly being pushed further away from the cylinder surface at a rate which reflects the growth of the boundary-layer. For this reason we are justified in saying that the vorticity, by the mechanism of convection, does not reach the outer boundary ξ_∞.

We solve for the stream function by expanding it into a Fourier series given by

$$\Psi(z, \theta, t) = \tfrac{1}{2}F_0(z, t) + \sum_{n=1}^{\infty}[F_n(z, t) \cos n\theta + f_n(z, t) \sin n\theta]. \tag{29}$$

This then transforms Equation (22) into the following sets of equations for F_n and f_n, which at a given time t can be viewed as ordinary differential equations

$$\frac{\partial^2 f_n}{\partial z^2} - n^2\lambda^2 f_n = r_n(z, t); \quad n = 1, 2, \ldots, \tag{30}$$

$$\frac{\partial^2 F_n}{\partial z^2} - n^2\lambda^2 F_n = s_n(z,t); \quad n = 0, 1, \ldots, \tag{31}$$

where the functions $r_n(z,t)$ and $s_n(z,t)$ are defined as

$$r_n(z,t) = \frac{1}{\pi}\int_0^{2\pi} H^2\omega \sin n\theta \, \mathrm{d}\theta; \quad n = 1, 2, \ldots, \tag{32}$$

$$s_n(z,t) = \frac{1}{\pi}\int_0^{2\pi} H^2\omega \cos n\theta \, \mathrm{d}\theta; \quad n = 0, 1, \ldots. \tag{33}$$

Boundary conditions for F_n and f_n can be obtained by the no-slip condition which can be restated as

$$\Psi = 0, \qquad \frac{\partial \Psi}{\partial z} = 0 \quad \text{on } z = 0 \tag{34}$$

and the far-field condition (28). Hence, we find that

$$F_0(0,t) = 0, \qquad F_n(0,t) = 0, \qquad f_n(0,t) = 0, \tag{35}$$

$$\frac{\partial F_0}{\partial z} = 0, \qquad \frac{\partial F_n}{\partial z} = 0, \qquad \frac{\partial f_n}{\partial z} = 0 \quad \text{on } z = 0 \quad \text{for all } t, \tag{36}$$

$$\exp(-\lambda z)F_0 \to 0, \qquad \exp(-\lambda z)F_n \to \frac{1}{2\lambda}\exp(\xi_0)\sin\alpha(t)\delta_{1,n},$$

$$\exp(-\lambda z) f_n \to \frac{1}{2\lambda}\exp(\xi_0)\cos\alpha(t)\delta_{1,n}, \quad \text{as } z \to \infty, \tag{37}$$

and

$$\exp(-\lambda z)\frac{\partial F_0}{\partial z} \to -\frac{\dot{\alpha}(t)}{2}\exp(\lambda z + 2\xi_0),$$

$$\exp(-\lambda z)\frac{\partial F_n}{\partial z} \to \tfrac{1}{2}\exp(\xi_0)\sin\alpha(t)\delta_{1,n},$$

$$\exp(-\lambda z)\frac{\partial f_n}{\partial z} \to \tfrac{1}{2}\exp(\xi_0)\cos\alpha(t)\delta_{1,n} \quad \text{as } z \to \infty \tag{38}$$

for $n = 1, 2, \ldots$ and $\delta_{1,n}$ is the Kronecker delta defined by

$$\delta_{1,n} = \begin{cases} 1 & \text{if } n = 1 \\ 0 & \text{if } n \neq 1 \end{cases}. \tag{39}$$

Further conditions satisfied by the functions $r_n(z,t)$ and $s_n(z,t)$ can be obtained by considering the properties of the solutions to Equations (30), (31) together with their corresponding boundary conditions (35)–(38). These conditions are of a global or integral nature and are

exact; they also play an important role in the determination of the surface vorticity and are given by

$$\int_0^\infty \exp(-n\lambda z) r_n(z,t)\,\mathrm{d}z = \exp(\xi_0)\,\cos\,\alpha(t)\delta_{1,n}, \tag{40}$$

$$\int_0^\infty \exp(-n\lambda z) s_n(z,t)\,\mathrm{d}z = \exp(\xi_0)\,\sin\,\alpha(t)\delta_{1,n}, \tag{41}$$

$$\int_0^{z_\infty} s_0(z,t)\,\mathrm{d}z = -\frac{\dot{\alpha}(t)}{2}\,\exp(2(\xi_0+\lambda z_\infty)). \tag{42}$$

The use of integral conditions in a numerical scheme is also used in the studies of Dennis and Staniforth [14], Collins and Dennis [15] and Badr and Dennis [17] to mention a few.

Equations (30), (31) at a fixed value of t are of the form

$$h''(z) - \beta^2 h(z) = g(z), \tag{43}$$

where $\beta = n\lambda$ and the prime refers to differentiation with respect to z. We may integrate these ordinary differential equations using step-by-step formulae. The important point to note here is that the particular marching algorithm to be used is dependent on the parameter β. Dennis and Chang [26] have found that most step-by-step procedures become increasingly unstable as β becomes large. Hence, two sets of step-by-step methods were utilized: one for $\beta < 0{\cdot}5$ while another for $\beta \geqslant 0{\cdot}5$. The specific schemes used will not be presented; however, these details can be found in Staniforth [8].

Equation (23) is solved by finite differences. Previous studies for the case of a circular cylinder have also expanded the vorticity in a Fourier series. In this instance the metric given by $H^2 = e^{2\xi}$ is independent of θ. In our problem the metric, given by Equation (13), depends on θ and, consequently, complicates matters greatly if expressed in a Fourier series. Despite this, Patel [16] for the case of a stationary inclined elliptic cylinder expanded the vorticity in a Fourier series and numerically solved the resulting partial differential equations for the Fourier coefficients.

The scheme used to approximate Equation (23) is very similar to the Crank–Nicolson implicit procedure. Equation (23) may be rewritten in the form

$$t\frac{\partial\omega}{\partial t} = q(z,\theta,t), \tag{44}$$

where

$$\begin{aligned} q(z,\theta,t) \;=\; & \frac{1}{4H^2}\frac{\partial^2\omega}{\partial z^2} + \frac{z}{2}\frac{\partial\omega}{\partial z} + \frac{\omega}{2} + \frac{\lambda^2}{4H^2}\frac{\partial^2\omega}{\partial\theta^2} \\ & + \frac{t}{H^2}\left(\frac{\partial\Psi}{\partial\theta}\frac{\partial\omega}{\partial z} - \frac{\partial\Psi}{\partial z}\frac{\partial\omega}{\partial\theta}\right) - 2\lambda t\ddot{\alpha}. \end{aligned} \tag{45}$$

It is the finite-difference approximation to the time derivative that enables us to advance the solution step-by-step in time. Assuming the solution at time t is known, let us advance the solution to time $t + \Delta t$ by integrating Equation (44). Integration by parts yields

$$\omega\tau\big|_t^{t+\Delta t} - \int_t^{t+\Delta t} \omega\,\mathrm{d}\tau = \int_t^{t+\Delta t} q\,\mathrm{d}\tau, \tag{46}$$

where Δt is the time increment. If we approximate the integrals using the trapezoidal rule this brings us to the expression

$$\omega(z, \theta, t + \Delta t) = \omega(z, \theta, t) + \left(\frac{\Delta t}{2t + \Delta t}\right)[q(z, \theta, t + \Delta t) + q(z, \theta, t)]. \tag{47}$$

Since $q(z, \theta, t + \Delta t)$ depends on $\omega(z, \theta, t + \Delta t)$ and its derivatives the scheme is implicit. Equation (47) is solved iteratively using the Gauss–Seidel procedure. All spatial derivatives appearing in (45) are approximated using central differences.

The boundary conditions used in solving the vorticity transport equation include

$$\omega(z, \theta, t) = \omega(z, \theta + 2\pi, t) \tag{48}$$

and

$$\omega(z_\infty, \theta, t) = -2\lambda\dot{\alpha}. \tag{49}$$

The surface vorticity is determined by inverting (32), (33); this leads to the following expression

$$\omega(0, \theta, t) = \frac{1}{H_0^2}\left\{\tfrac{1}{2}s_0(0, t) + \sum_{n=1}^{\infty}[r_n(0, t)\ \sin\ n\theta + s_n(0, t)\ \cos\ n\theta]\right\}. \tag{50}$$

To initiate the integration procedure, the solution at $t = 0$ must be known. Setting $t = 0$, and hence $\lambda = 0$, in Equations (22), (23) yields

$$\frac{\partial^2\Psi}{\partial z^2} = H_0^2\omega, \tag{51}$$

$$\frac{1}{H_0^2}\frac{\partial^2\omega}{\partial z^2} + 2z\frac{\partial\omega}{\partial z} + 2\omega = 0. \tag{52}$$

The exact solution to Equations (51), (52) satisfying all the boundary conditions is given by

$$\omega(z, \theta, 0) = \frac{2}{\sqrt{\pi}H_0}\ \exp(\xi_0 - H_0^2z^2)\ \sin(\theta + \alpha(0)), \tag{53}$$

$$\Psi(z, \theta, 0) = \frac{\exp(\xi_0)}{H_0}\left[H_0z\ \mathrm{erf}(H_0z) + \frac{1}{\sqrt{\pi}}(\exp(-H_0^2z^2) - 1)\right]\sin(\theta + \alpha(0)) \tag{54}$$

where $\mathrm{erf}(H_0z)$ denotes the error function.

We summarize the numerical method by listing the numerical procedure. Assuming all quantities are known at time t and realising that we wish to advance the solution a time $t + \Delta t$, we perform the following steps (k denotes the iteration counter):

(1) solve for $\omega^{(k)}(z, \theta, t + \tau)$ using (47) everywhere except on the cylinder surface ($z = 0$),
(2) compute $r_n^{(k)}(z, t + \tau)$, $_n^{(k)}(z, t + \tau)$ from (32), (33) for $z \neq 0$,
(3) calculate $r_n^{(k)}(0, t + \tau)$, $s_n^{(k)}(0, t + \tau)$ by enforcing the integral conditions (40)–(42) and hence compute $\omega^{(k)}(0, \theta, t + \tau)$ from (50),

(4) solve Equations (30), (31) for $f_n^{(k)}(z, t+\tau)$, $F_n^{(k)}(z, t+\tau)$ and thus obtain $\Psi^{(k)}(z, \theta, t+\tau)$ using (29), and
(5) repeat above steps till convergence is reached and increment k by 1 after each complete iteration.

Step (3) indicates how the integral conditions are used in determining the surface vorticity. It may also be necessary to subject the surface vorticity to under-relaxation in order to obtain convergence. Convergence is reached when the difference between two successive iterates of the surface vorticity, $|\omega^{(k+1)}(0, \theta, t) - \omega^{(k)}(0, \theta, t)|$, falls below some specified tolerance ε. Typically, $\varepsilon = 10^{-6}$ was used. Lastly, we point out that the integrals appearing in (32), (33) were evaluated by Filon integration in order to guarantee consistent accuracy for all n. This technique bears a close resemblance to Simpson's rule with the exception that only the unknown part of the integrand is approximated by a parabola over three successive grid points rather than the entire integrand.

5. Results

The flow is characterized by the following dimensionless parameters: Re, r, α_0, δ, f. By the choice of $\alpha(t)$ many cases can be considered. For example, $\alpha(t) = \alpha_0$ for the stationary case while $\alpha(t) = 2\pi f t$ for the pure rotational case. Runs were carried out for Reynolds numbers 500 and 1,000 spanning at least two complete cycles. A thin ellipse having $\hat{r} = 0{\cdot}1$ oscillating at a frequency $f = 0{\cdot}5$ was considered. The remaining parameters were varied in order to determine their effect on the flow. Since all cases considered have $f = 0{\cdot}5$, or $T = 2$, and $\delta \geqslant 0$ a complete cycle consists of the following four stages. In the initial stage, $0 < t \leqslant 0{\cdot}5$, the ellipse starts out at its lowest inclination, $\alpha_0 - \delta$, and its rate of oscillation, $\dot{\alpha}$, increases from zero to its maximum value $2\pi f \delta$ at $t = 0{\cdot}5$ where $\alpha(0{\cdot}5) = \alpha_0$. During the second stage where $0{\cdot}5 < t \leqslant 1$ the ellipse's inclination continues to increase to its maximum value, $\alpha_0 + \delta$, at $t = 1$; however, $\dot{\alpha}$ decreases steadily to zero during this time interval. Then for $1 < t \leqslant 1{\cdot}5$ the inclination begins to decrease and assumes a value of α_0 at $t = 1{\cdot}5$ while $\dot{\alpha}$ increases from zero to its maximum value at $t = 1{\cdot}5$. In the final stage where $1{\cdot}5 < t \leqslant 2$ the inclination continues to decrease to its minimum value at $t = 2$, thus completing one cycle. The oscillation rate decreases from its maximum value to zero during this final interval.

Before presenting the numerical results we first test our numerical scheme against existing results for the purely translating case with Re = 5,000, $\alpha = \pi/12$ and $\hat{r} = 0{\cdot}6$. To demonstrate convergence computations were carried out on three different grids: a fine grid having $N \times M = 201 \times 161$, an intermediate grid with $N \times M = 151 \times 121$ and a coarse grid of $N \times M = 101 \times 81$. Displayed in Figures 1a and 1b are the time variations in the drag and lift coefficients, C_D and C_L, respectively. We computed the drag and lift coefficients using the formulae

$$X_P = \frac{2 \sinh \xi_0}{\mathrm{Re}} \int_0^{2\pi} \left(\frac{\partial \zeta}{\partial \xi}\right)_0 \sin(\theta)\, \mathrm{d}\theta,$$

$$X_F = -\frac{2 \cosh \xi_0}{\mathrm{Re}} \int_0^{2\pi} \zeta_0 \sin(\theta)\, \mathrm{d}\theta,$$

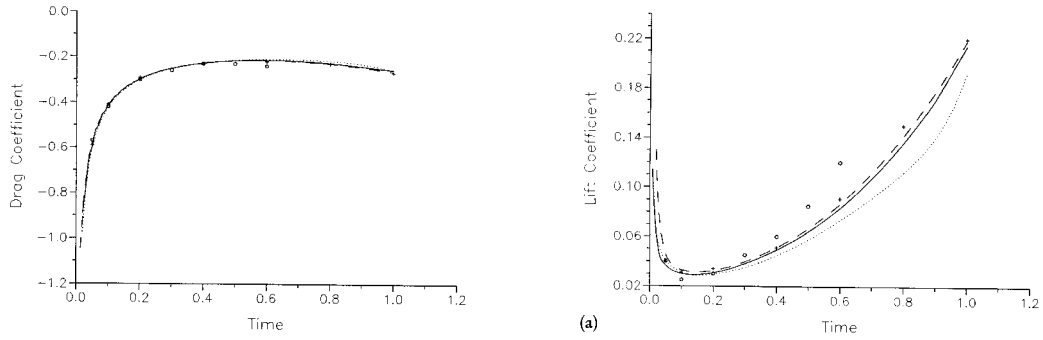

(a) (b)

Figures 1(a–b). Variation of the (a) drag and (b) lift coefficients with time using the grids $N \times M = 101 \times 81$ (dotted line), $N \times N = 151 \times 121$ (dashed line) and $N \times M = 201 \times 161$ (solid line) for the case Re = 5,000, $\hat{r} = 0{\cdot}6$ and $\alpha = \frac{\pi}{12}$. Also shown are results obtained by Staniforth [8] using a numerical procedure (crosses) and a series solution (circles).

$$Y_P = -\frac{2\cosh\xi_0}{\mathrm{Re}} \int_0^{2\pi} \left(\frac{\partial\zeta}{\partial\xi}\right)_0 \cos(\theta)\,\mathrm{d}\theta,$$

$$Y_F = \frac{2\sinh\xi_0}{\mathrm{Re}} \int_0^{2\pi} \zeta_0 \cos(\theta)\,\mathrm{d}\theta.$$

Defining $X = X_P + X_F$ and $Y = Y_P + Y_F$ we then arrive at

$$C_D = X\cos(\alpha(t)) - Y\sin(\alpha(t)), \tag{55}$$

$$C_L = Y\cos(\alpha(t)) + X\sin(\alpha(t)). \tag{56}$$

Also shown in the diagrams are the values obtained by Staniforth [8] using both a numerical procedure as well as a series solution which is valid for small times. We point out that at $t = 0$ both C_D and C_L are infinite in magnitude due to the fact that the cylinder experiences infinite acceleration at that time and then decreases rapidly. For this reason C_D and C_L are plotted for $t > 0{\cdot}01$. Figure 1a illustrates very good agreement in C_D and shows little dependence on the grid used while Figure 1b reveals that the computation of C_L does show some dependence on the grid size. However, very little is gained in going from the intermediate grid to the fine grid. Also, the results obtained agreed well with those of Staniforth. As expected, the series solution for C_L departs from the numerical solution as time increases.

The remaining computations were carried out using the intermediate grid of $N \times M = 151 \times 121$. Other computational parameters used include an outer boundary of $z_\infty = 8$, a relaxation parameter in the range $0{\cdot}1 \leqslant \kappa \leqslant 0{\cdot}5$, and 20 terms of the Fourier series. The number of terms retained in the Fourier series was determined by experimenting with the exact initial solution for the stream function. It was found that the number of terms in the series was adequate for all times considered. Because of the impulsive start, small time steps were needed to get past the singularity at $t = 0$. In order to get an estimate on a reasonable initial time step the stability condition

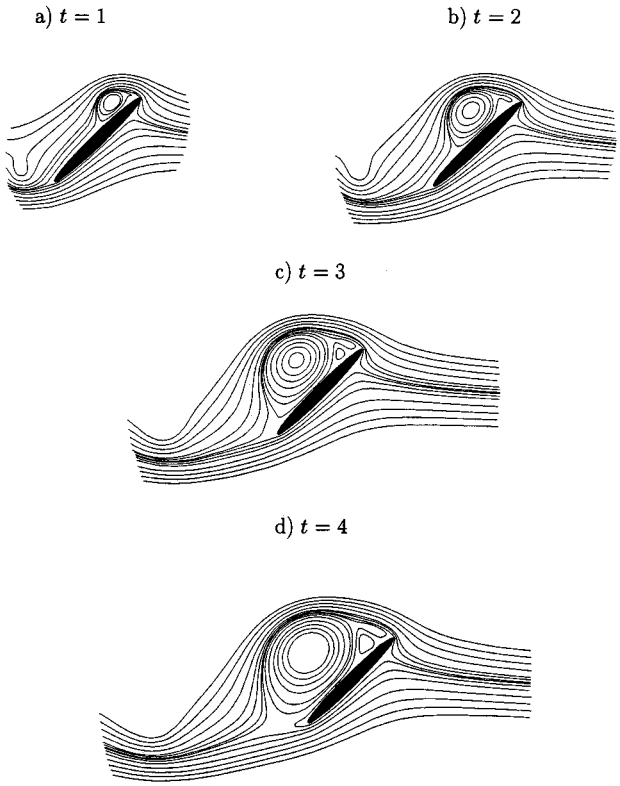

Figures 2(a–d). Streamline plots for the case Re $=$ 500, $\hat{r} = 0{\cdot}1$ and $\alpha = \frac{\pi}{4}$ at times (a) $t = 1$, (b) $t = 2$, (c) $t = 3$ and (d) $t = 4$.

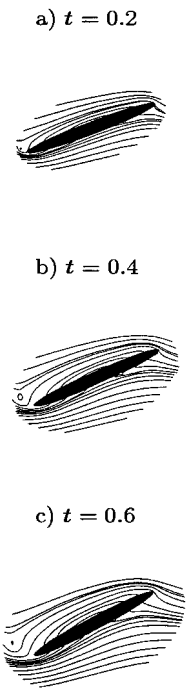

Figure 3(a–c). Streamline plots for the case Re $=$ 500, $\hat{r} = 0{\cdot}1$ and $\alpha = \frac{\pi}{6} - \frac{\pi}{30}\cos(\pi t)$ at early times (a) $t = 0{\cdot}2$, (b) $t = 0{\cdot}4$, and (c) $t = 0{\cdot}6$.

$$\Delta t \leqslant \frac{\mathrm{Re}\, H_m^2 h^2}{4}$$

was used. This condition results from Equation (19) which states that for early times the problem can be treated as a simple heat conduction equation with the nonlinear terms neglected and with H assuming its minimum value on the surface, H_m. The time step implied by this condition represents an upper bound required initially. The quantity H_m^2 is given by

$$H_m^2 = \frac{\cosh(2\xi_0) - 1}{2}$$

and $h = z_\infty / N$, thus we arrive at

$$\Delta t \leqslant \frac{\mathrm{Re}(\cosh(2\xi_0) - 1) z_\infty^2}{8N^2}.$$

For $z_\infty = 8$, $N = 161$, Re ≈ 100 and $\tanh \xi_0 = 0{\cdot}1$ we find that $\Delta t \leqslant 0{\cdot}0006$. From this crude estimate we decided to proceed initially with time steps of 10^{-4} for the first 10 advances. Once the solution had evolved past the initial singular stage it was observed that the time step

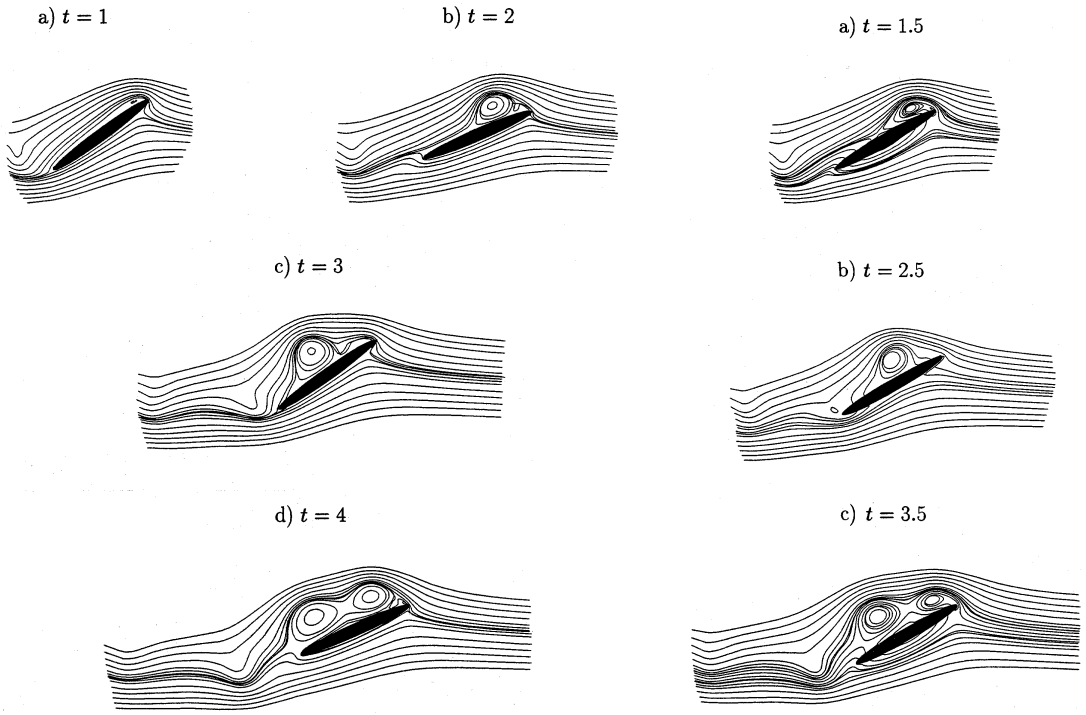

Figures 4(a–d). Streamline plots for the case Re $=$ 500, $\hat{r} = 0{\cdot}1$ and $\alpha = \frac{\pi}{6} - \frac{\pi}{30}\cos(\pi t)$ at times (a) $t = 1$, (b) $t = 2$, (c) $t = 3$ and (d) $t = 4$.

Figures 5(a–c). Streamline plots for the case Re $=$ 500, $\hat{r} = 0{\cdot}1$ and $\alpha = \frac{\pi}{6} - \frac{\pi}{30}\cos(\pi t)$ at intermediate times (a) $t = 1{\cdot}5$, (b) $t = 2{\cdot}5$, (c) $t = 3{\cdot}5$.

could be increased substantially. For example, the next 10 time steps were proceeded with $\Delta t = 10^{-3}$ and continued after with $\Delta t = 10^{-2}$. Clearly, this time step can be increased by working with a coarser grid. We emphasize that no stability difficulties were encountered with the choice of grids and parameters listed above. In order to plot the streamlines in the inertial reference frame we must relate it to its counterpart in the rotating reference frame. This is done through the expression

$$\psi_I = \psi_R + \tfrac{1}{2}\dot{\alpha}(t)r^2,$$

where the subscript I denotes the inertial frame while R denotes the rotating frame and r refers to the polar radius, $r^2 = x^2 + y^2$. Similarly, the vorticities are related through the expression

$$\zeta_I = \zeta_R + 2\dot{\alpha}(t).$$

To establish the dependence of the flow on the parameters Re, α_0 and δ we present the flow patterns in the following systematic order. In all flow patterns to be presented, the direction of the flow is from right to left. We begin with the stationary case Re $= 500$, $\alpha_0 = \pi/4$ and $\delta = 0$. Next, we discuss the results for Re $= 500$, $\alpha_0 = \pi/6$, $\delta = \pi/30$. Following this we consider the case Re $= 1{,}000$, $\alpha_0 = \pi/6$, $\delta = \pi/30$ to illustrate the dependence on the Reynolds number. Lastly, we present the case with Re $= 500$, $\alpha_0 = \pi/4$, $\delta = \pi/12$ to portray the effect of increasing both the inclination and the amplitude of oscillation and also to bring out the effect of oscillation.

Shown in Figure 2 are four snap shots of the flow field at times $t = 1, 2, 3, 4$ for the purely translating case with Re $= 500$, $\hat{r} = 0{\cdot}1$ and $\alpha(t) = 45°$. At $t = 1$ Figure 2a shows vortices ocurring at the leading edge. Also evident from this diagram, yet less apparent, is that vortex shedding has already taken place. This is evidenced by the wavy streamline behind the trailing edge. As the time is increased to $t = 2$ we see that the shed vortex has been convected further downstream while the vortices at the leading edge grow. Figures 2c, d for times $t = 3, 4$ respectively reveal that the vortices at the leading edge continue to grow and eventually span the entire top side of the ellipse. While secondary vortices are shown to be forming at the leading edge no new vortices are shed off the trailing edge. As a final observation, we note that as the shed vortex continues to travel downstream it becomes weaker.

Illustrated in Figures 3–5 are instantaneous streamline patterns for the case Re $= 500$, $\hat{r} = 0{\cdot}1$ and $\alpha(t) = \pi/6 - \pi/30\cos(\pi t)$; thus, the ellipse is oscillating about an average inclination of 30° with an amplitude of oscillation of $\pm 6°$. Figure 3 confirms that the trailing vortex is formed and shed early in the first half of the cycle while Figures 3c and 4a verify that the leading vortex is formed later on in the first half during the time when the ellipse is decelerating in an upward motion and before it attains its maximum inclination. Figure 4c at $t = 3$ reveals that another vortex has been shed from the trailing edge early in the second cycle of oscillation. Portrayed in Figures 5a, b, c are intermediate flow patterns at times $t = 1{\cdot}5, 2{\cdot}5, 3{\cdot}5$, respectively. These correspond to instants when the rate of oscillation is maximum and the ellipse assumes its average inclination. In Figures 5a,c the ellipse is descending while in Figure 5b it is ascending. While ascending or descending fluid is forced to flow around the leading and trailing tips of the ellipse. When descending the vortices formed at the leading edge are strengthened. On the other hand, when ascending the secondary vortices formed at the leading edge temporarily disappear and reappear just before the ellipse reaches its maximum inclination.

In Figure 6 the Reynolds number is increased to Re $= 1{,}000$ while the inclination is the same as in the previous case. In comparing Figure 6 with Figure 4 we see that increasing the Reynolds number from 500 to 1,000 has little effect as both plots share many similarities. One of which is that the primary vortex formed at the leading edge moves slightly along the top surface of the cylinder towards the trailing edge. Differences in size of the vortices at the leading edge are noticed at $t = 1$ as well as the distance that the shed vortex has travelled downstream.

We now discuss the case Re $= 500$, $\hat{r} = 0{\cdot}1$ and $\alpha(t) = \pi/4 - \pi/12\cos(\pi t)$; here the ellipse is oscillating about an average inclination of 45° with an amplitude of oscillation of $\pm 15°$. This corresponds to the case known as deep stall. Streamline patterns are included in Figures 7–11. Comparing Figure 2 (the stationary case with $\alpha = \pi/4$) with Figure 8 we see that the flow features are essentially the same at times $t = 1$ and $t = 2$. Marked differences become apparent at times $t = 3$ and $t = 4$ since vortex shedding occurs again for the oscillating case. Each oscillation of the ellipse appears to provoke vortex shedding. Thus an obvious effect of oscillation is to induce vortex shedding from the trailing edge. This effect superposes itself on the usual vortex development around a purely translating elliptic cylinder. The resulting flow pattern depends on the relative strength and synchronization of these two vortex processes. Another difference lies in the way the primary and secondary vortices at the leading edge interact with one another. In the stationary case these vortices remain separated whereas in the oscillating case they begin to merge. To determine the effect of increasing both the average inclination and the amplitude of oscillation we compare Figures 7–11 with

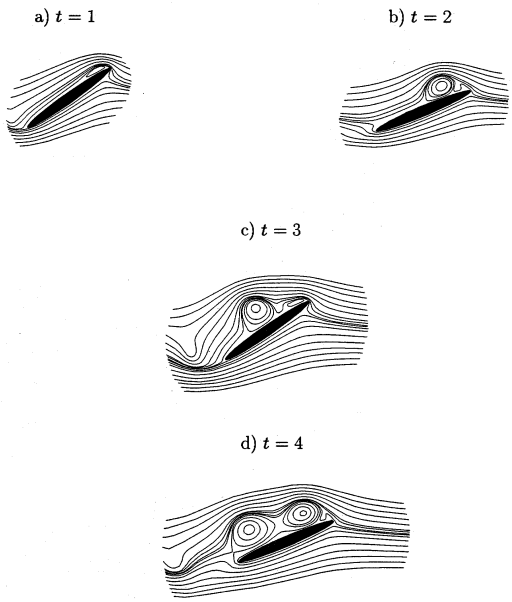

Figures 6(a–d). Streamline plots for the case Re = 1,000, $\hat{r} = 0{\cdot}1$ and $\alpha = \frac{\pi}{6} - \frac{\pi}{30}\cos(\pi t)$ at times (a) $t = 1$, (b) $t = 2$, (c) $t = 3$ and (d) $t = 4$.

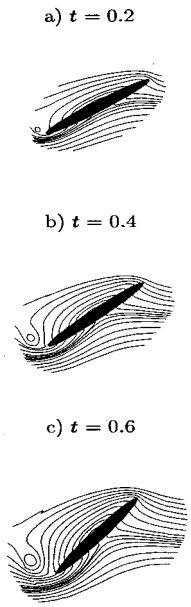

Figures 7(a–c). Streamline plots for the case Re = 500, $\hat{r} = 0{\cdot}1$ and $\alpha = \frac{\pi}{4} - \frac{\pi}{12}\cos(\pi t)$ at early times (a) $t = 0{\cdot}2$, (b) $t = 0{\cdot}4$, (c) $t = 0{\cdot}6$.

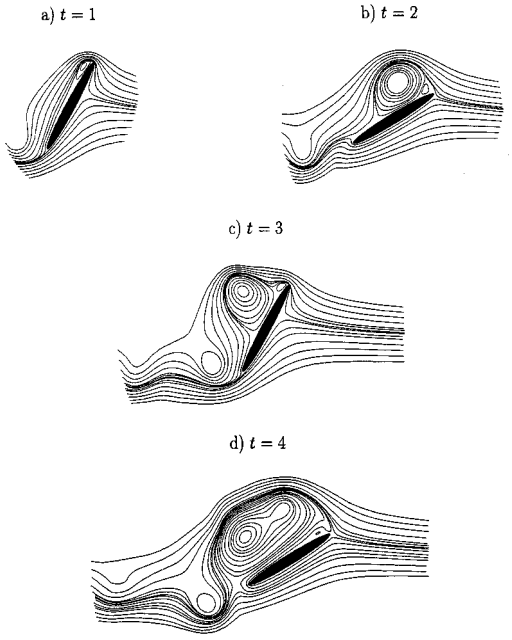

Figures 8(a–d). Streamline plots for the case Re = 500, $\hat{r} = 0{\cdot}1$ and $\alpha = \frac{\pi}{4} - \frac{\pi}{12}\cos(\pi t)$ at times (a) $t = 1$, (b) $t = 2$, (c) $t = 3$ and (d) $t = 4$.

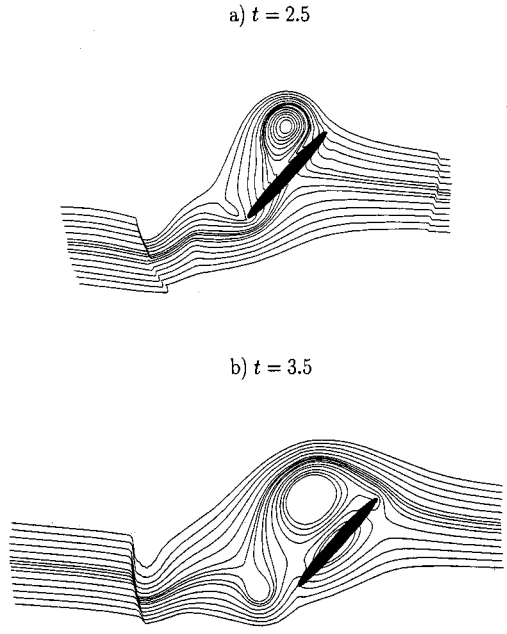

Figures 9(a–b). Streamline plots for the case Re = 500, $\hat{r} = 0{\cdot}1$ and $\alpha = \frac{\pi}{4} - \frac{\pi}{12}\cos(\pi t)$ at intermediate times (a) $t = 2{\cdot}5$, (b) $t = 3{\cdot}5$.

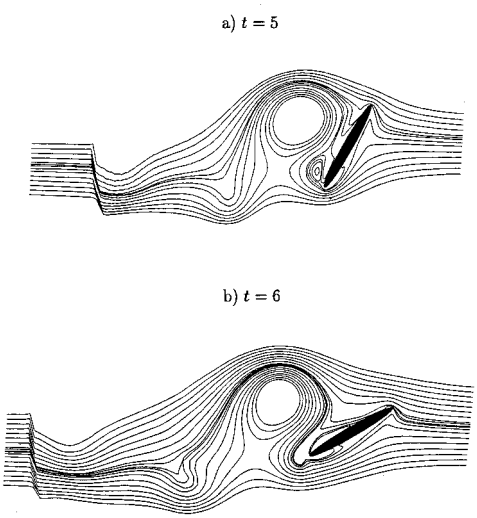

Figures 10(a–b). Streamline plots for the case Re $= 500$, $\hat{r} = 0{\cdot}1$ and $\alpha = \frac{\pi}{4} - \frac{\pi}{12}\cos(\pi t)$ at later times (a) $t = 5$, (b) $t = 6$.

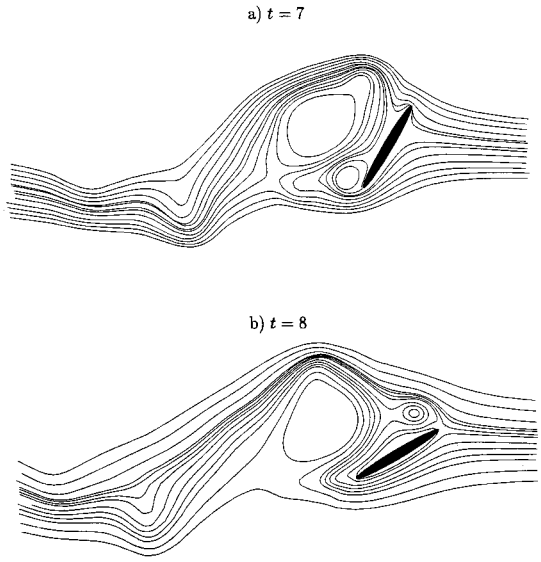

Figures 11(a–b). Streamline plots for the case Re $= 500$, $\hat{r} = 0{\cdot}1$ and $\alpha = \frac{\pi}{4} - \frac{\pi}{12}\cos(\pi t)$ at larger times (a) $t = 7$, (b) $t = 8$.

Figures 3–5. Doing this we find that the vortices at the leading edge grow at a faster rate. At $t = 4$ in Figure 8d the merged vortices are forced to shed off the top surface and new vortices are forming at the leading edge. The quick shedding of the vortices from the top surface is due to having such a large amplitude of oscillation. Shown in Figures 9a, b are the flow patterns at the intermediate times of $t = 2{\cdot}5, 3{\cdot}5$ when the ellipse is ascending and descending respectively. The forced flow around the tips of the ellipse is more evident in these figures than in those illustrated in Figure 5. In addition we present plots for larger times $t = 5, 6$ in Figures 10a,b, respectively, and times $t = 7, 8$ in Figures 11a,b respectively. Figures 10a and 11a indicate that vortices have been formed and shed from the trailing edge therefore suggesting that the frequency at which vortices are shed is equal to the frequency of oscillation of the ellipse. In the literature this occurrence is referred to as lock-in and has significant consequences on the drag and lift and on the power transfer between the body and the fluid. These figures show that the shed merged vortices from the top surface have now formed a single vortex and is being carried downstream. As they travel downstream they weaken. This is evidenced by the fact that close to the ellipse vortices are observed as closed streamlines whereas further away they are observed as wavy streamlines. The step-like distortions in the streamlines shown in Figures 9 and 10 indicate that there is a sharp transition separating the essentially unaffected uniform far-field flow from the region closer to the cylinder most influenced by the expanding boundary layer and vortex shedding process. Lastly, as already mentioned, the plots for $t = 7, 8$ reinforce the observation that the descending movement of the leading edge induces vortices to form at the leading edge while ascending motion freezes further development.

Finally, included in Figures 12a, b are vorticity contour plots for the case Re $= 500$, $\hat{r} = 0{\cdot}1$ and $\alpha(t) = \pi/4 - \pi/12\cos(\pi t)$ at times $t = 7, 8$ respectively. The various closed curves observed in these diagrams confirm the ongoing vortex shedding process and also how quickly

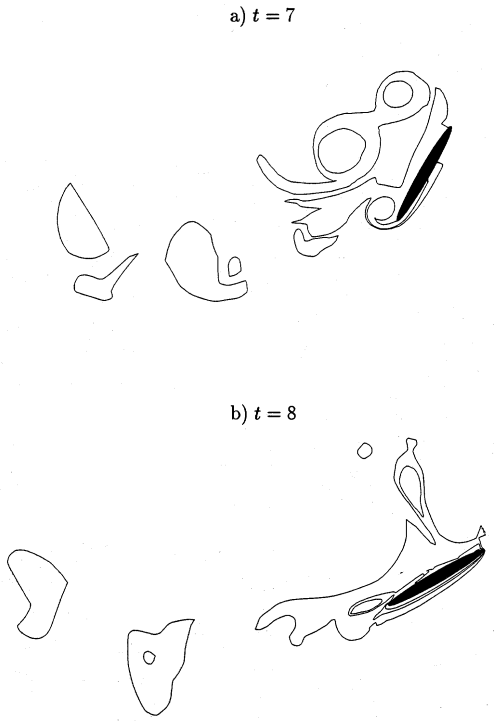

Figures 12(a–b). Vorticity contour plots for the case Re $= 500$, $\hat{r} = 0{\cdot}1$ and $\alpha = \frac{\pi}{4} - \frac{\pi}{12}\cos(\pi t)$ at times (a) $t = 7$ and (b) $t = 8$.

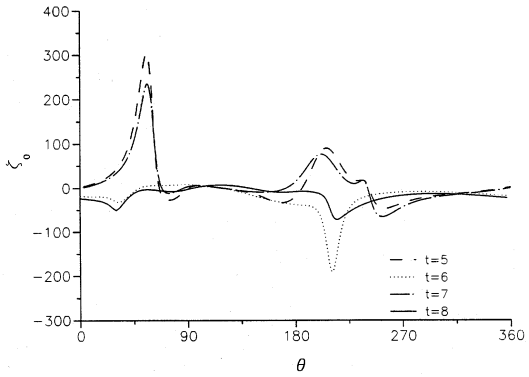

Figure 13. Surface vorticity distribution for the case Re $= 500$, $\hat{r} = 0{\cdot}1$ and $\alpha = \frac{\pi}{4} - \frac{\pi}{12}\cos(\pi t)$ at times $t = 5, 6, 7, 8$.

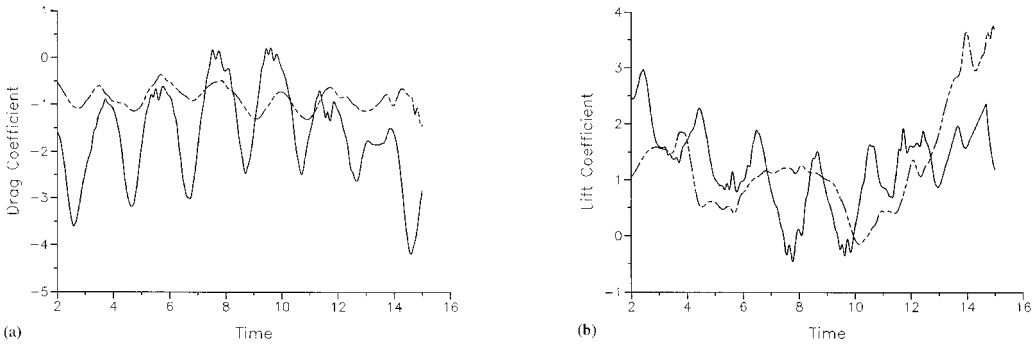

Figures 14(a–b). Variation of the (a) drag and (b) lift coefficients with time for the cases Re $= 500$, $\hat{r} = 0{\cdot}1$, $\alpha = \frac{\pi}{4} - \frac{\pi}{12}\cos(\pi t)$ (solid line) and Re $= 1{,}000$, $\hat{r} = 0{\cdot}25$, $\alpha = \frac{\pi}{6} - \frac{\pi}{45}\cos(\pi t)$ (dashed line).

the magnitude of the vorticity decays with downstream distance. The furthest closed contour is approximately an order of magnitude less than the contour closest to the cylinder. The corresponding surface vorticity distributions at times $t = 5, 6, 7, 8$ are illustrated in Figure 13. These plots reveal rapid variations in the vicinity of the tips of the ellipse located at $\theta = \alpha, 180^\circ + \alpha$. Also indicated in these plots is that the sense of rotation when the ellipse is at its maximum inclination is opposite to that at its lowest inclination. The strength of the vorticity is greatest at the leading tip when the ellipse is at its maximum inclination and the situation reverses when the minimum inclination is reached. The diagram also suggests that

a periodic pattern in the surface vorticity distribution may be emerging. Since the forcing is periodic it is natural to assume that a periodic flow results. To pursue this possibility further, runs were carried out for larger times. In Figures 14a, b drag and lift coefficients are plotted respectively for the cases Re $= 500$, $\hat{r} = 0{\cdot}1$, $\alpha = \frac{\pi}{4} - \frac{\pi}{12}\cos(\pi t)$ and Re $= 1,000$, $\hat{r} = 0{\cdot}25$, $\alpha = \frac{\pi}{6} - \frac{\pi}{45}\cos(\pi t)$. Not shown in these plots are the variations in C_D and C_L during the first cycle since they change rapidly over several orders of magnitude during this interval. Figure 14a shows that the drag coefficient does reveal an almost periodic variation; however, the corresponding plot for the lift coefficient is not as suggestive. Judging from this, it maybe that the flow never settles down to a periodic state at these Reynolds numbers. The variations also indicate bursts of rapid fluctuations occurring in both C_D and C_L at similar instants when the ellipse is near its minimum inclination. In another study, D'Alessio [27] has shown that a periodic pattern in C_D and C_L does emerge for Re > 20 for the stationary case while for Re $\leqslant 20$ the drag and lift coefficients asymptotically approach their steady state values.

6. Conclusions

Considered in this paper is the unsteady two-dimensional flow of a viscous incompressible fluid past an impulsively started oscillating and translating elliptic cylinder. Due to the impulsive start of the motion, a singularity results in the vorticity. To remove this singularity and to stretch the thin boundary-layer a transformation was introduced. This boundary-layer type transformation incorporates the known early structure of the flow into the equations of motion.

A numerical method was described which is successful in computing the early stages of the flow immediately following the impulsive start for the Reynolds numbers of 500 and 1,000. Illustrated in the streamline plots are the features of vortex formation and vortex shedding from the leading and trailing edges of the ellipse. The effects of oscillation have been qualitatively described by comparisons with the corresponding translating case. The main difference observed deals with the rate at which vortices are shed from the trailing edge. For the oscillating case this frequency equals the oscillation frequency experienced by the ellipse for the cases considered. The flow patterns revealed that each oscillation provoked a rolling-up of the fluid successively around the leading and trailing edges of the ellipse. Also, the dependence of the flow on the average inclination and amplitude of oscillation was investigated. It appears that having a larger average inclination and amplitude of oscillation promotes the growth of vortices formed at the leading edge and forces them to be subsequently shed off the top surface of the ellipse. Further, it was observed that increasing the Reynolds number from 500 to 1,000 had little effect. Lastly, the results predicted by our numerical method have been tested against existing results for the stationary case. Good agreement with these results was found.

Acknowledgement

Financial support for this research was provided by the Natural Sciences and Engineering Research Council of Canada.

References

1. H. Blasius, Grenzschichten in Flüssigkeiten mit kleiner Reibung. *Zeits. Math. u Phys.* 56 (1908) 1–37. (English Translation NACA TM 1256).
2. S. Goldstein and L. Rosenhead, Boundary layer growth. *Proc. Camb. Phil. Soc.* 32 (1936) 392–401.

3. H. Schuh, Calculation of unsteady boundary layers in two-dimensional laminar flow. *Zeits. Flugwiss.* 1 (1953) 122–131.
4. H. Wundt, Wachstum der laminaren Grenzschicht an schräg angeströmtem Zylindern bei Anfahrt aus der Ruhe. *Ing. Arch.* 23 (1955) 212–230.
5. E. J. Watson, Boundary layer growth. *Proc. R. Soc. London A* 231 (1955) 104–116.
6. C.-Y. Wang, The flow past a circular cylinder which is started impulsively from rest. *J. Math. Phys.* 46 (1967) 195–202.
7. W. M. Collins and S. C. R. Dennis, The initial flow past an impulsively started circular cylinder. *Quart. J. Mech. Appl. Math.* 26 (1973) 53–75.
8. A. N. Staniforth, Ph.D. thesis, University of Western Ontario, London, Canada (1973) 201pp.
9. R. B. Payne, Calculations of unsteady viscous flow past a circular cylinder. *J. Fluid Mech.* 4 (1958) 81–86.
10. M. Kawaguti and P. Jain, *Numerical Study of a Viscous Fluid Past a Circular Cylinder*. University of Wisconsin, MRC Summary Report No. 590 (1965).
11. J. S. Son and T. J. Hanratty, Numerical solution for the flow around a cylinder at Reynolds numbers of 40, 200 and 500. *J. Fluid Mech.* 35 (1969) 369–386.
12. P. C. Jain and K. S. Rao, Numerical solution of unsteady viscous incompressible fluid flow past a circular cylinder. *The Physics of Fluids Supplement II* (1969) 57–64.
13. D. C. Thoman and A. A. Szewezyk, Numerical solutions of time dependent two-dimensional flow of a viscous, incompressible fluid over stationary and rotating cylinders. Heat Transfer and Fluid Mechanics. Laboratory, University of Notre Dame, Tech. Rep. 66–14, (1966).
14. S. C. R. Dennis and A. N. Staniforth, A numerical method for calculating the initial flow past a cylinder in a viscous fluid. In: M. Holt (ed.), *Proc. 2nd Int. Conf. Num. Meth. Fluid Dyn.*, Lecture Notes in Physics. Berlin: Springer-Verlag 8 (1971).
15. W. M. Collins and S. C. R. Dennis, Flow past an impulsively started circular cylinder. *J. Fluid Mech.* 60 (1973) 105–127.
16. V. A. Patel, Flow around the impulsively started elliptic cylinder at various angles of attack. *Comp. Fluids* 9 (1981) 435–462.
17. H. M. Badr and S. C. R. Dennis, Time-dependent viscous flow past an impulsively started rotating and translating circular cylinder. *J. Fluid Mech.* 158 (1985) 447–488.
18. H. J. Lugt and S. Ohring, Rotating elliptic cylinders in a viscous fluid at rest or in a parallel stream. *J. Fluid Mech.* 79 (1977) 127–156.
19. M. Coutanceau and R. Bouard, Experimental determination of the main features of the viscous flow in the wake of a circular cylinder in uniform translation. Part 2. Unsteady Flow. *J. Fluid Mech.* 79 (1977) 257–272.
20. R. Bouard and M. Coutanceau, The early stages of development of the wake behind an impulsively started cylinder for $40 < \mathrm{Re} < 10^4$. *J. Fluid Mech.* 101 (1980) 583–607.
21. M. Coutanceau and C. Menard, Influence of rotation on the near-wake development behind an impulsively started circular cylinder. *J. Fluid Mech.* 158 (1985) 399–446.
22. T. P. Loc, O. Daube, P. Monnet and M. Coutanceau, A comparison of numerical simulation and experimental visualization of the early stage of the flow generated by an impulsively started elliptic cylinder. In: C. Taylor, J. A. Johnson and W. R. Smith (eds), *Proc. 3rd Int. Conf. Num. Meth. in Laminar and Turbulent Flows.* Berlin: Springer-Verlag (1983) 269–279.
23. O. Daube, L. T. Thuoc, M. Coutanceau and P. Monnet, Numerical and experimental study of the viscous flow generated by an impulsively started elliptic cylinder. In: G. A. Keramidas and C. A. Brebbia (eds), *Computational Methods and Experimental Measurements*. Berlin: Springer-Verlag (1982) 763–773.
24. K. Ohmi, M. Coutanceau, T. P. Loc and A. Dulieu, Vortex formation around an oscillating and translating airfoil at large incidences. *J. Fluid Mech.* 211 (1990) 37–60.
25. K. Ohmi, M. Coutanceau, O. Daube and T. P. Loc, Futher experiments on vortex formation around an oscillating and translating airfoil at large incidences. *J. Fluid Mech.* 225 (1991) 607–630.
26. S. C. R. Dennis and Gau-Zu Chang, Numerical integration of the Navier-Stokes equations in two dimensions. Mathematics Research Center, University of Wisconsin, *Technical Summary Report* No. 859 (1969), 89pp.
27. S. J. D. D'Alessio, Steady, unsteady and linear stability of flow past an elliptic cylinder. *Can. Appl. Math. Q.* 4 (1996) 341–379.